actuators

MDPI

Article

A New Shaped Disturbance Observer to Improve Stability in a Time-Delayed Steering Control System for a Corner Module

Chenghao Sang [1], Zihong Li [2], Ning Zhang [2] and Hui Shen [1,*]

[1] School of Mechanical Engineering, Yangzhou University, Yangzhou 225009, China; mz120240942@stu.yzu.edu.cn
[2] School of Mechanical Engineering, Southeast University, Nanjing 211189, China; zihong_li@seu.edu.cn (Z.L.); nzhang_cn@seu.edu.cn (N.Z.)
* Correspondence: hshen@yzu.edu.cn

Abstract

Conventional disturbance observers improve disturbance rejection in steer-by-wire corner modules. However, feedback delay and higher observer gain strengthen the compensation–delay coupling, aggravating wheel-angle vibration and shrinking the closed-loop stability region. To address this conflict, a shaped disturbance observer is proposed. The shaped disturbance observer improves the estimation of time-varying wheel-end disturbance torque, while a shaping filter reconfigures the magnitude and phase characteristics of the compensation channel. Based on the corner module dynamics, a delay-dependent closed-loop characteristic equation is derived, and stability boundaries are evaluated using frequency-domain boundary curves and characteristic roots. With the observers tuned using a common nominal error-pole location, the shaped disturbance observer exhibits smaller estimation phase lag at all four tested frequencies, while its root mean square estimation error varies relative to that of the conventional disturbance observer with disturbance frequency. Under identical feedback delays, its stability region area is 8.3–91.4% larger than that of the conventional disturbance observer. Simulation results quantify the trade-offs among disturbance estimation accuracy, compensation bandwidth, and closed-loop stability.

Keywords: corner modules; delay-induced vibration; Shaped DOb; D-curve; characteristic roots; stability region

1. Introduction

With advances in vehicle electrification, intelligent driving, and chassis-by-wire technologies, distributed steer-by-wire systems have become a promising architecture for highly maneuverable vehicles [1,2]. By removing the mechanical linkages among wheels, independently actuated corner modules can track target angles assigned by a high-level motion controller, enabling four-wheel independent steering, yaw-motion regulation, and crab steering [3–5]. However, wheel-end actuators are affected by tire self-aligning torque, road impacts, friction, and parameter variations, while feedback delays arise from sensing, communication, and computation. These effects reduce tracking accuracy and may induce wheel-angle vibration or closed-loop instability. Because wheel angles directly affect tire lateral forces and vehicle yaw moment, vibration of a single corner module may disrupt coordinated multi-wheel steering [6–8].

Existing studies have mainly adopted feedforward, PID, sliding-mode, adaptive, and robust control methods [9–13]. Disturbance observers (DObs) estimate lumped disturbances from the nominal model, control input, and measured states and can be readily

Check for updates

Academic Editor: Arturo Zavala-Río

Received: 30 October 2026
Revised: 14 November 2026
Accepted: 16 November 2026
Published: 18 November 2026

Copyright: © 2026 by the authors. Licensee MDPI, Basel, Switzerland. This article is an open access article distributed under the terms and conditions of the Creative Commons Attribution (CC BY) license.

integrated into existing controllers. Conventional DObs generally assume locally constant disturbances, with their response governed by the observer gain L. Increasing L improves the observer bandwidth but also increases sensitivity to measurement noise and high-frequency dynamics [14–16]. In delayed steering systems, a higher L strengthens the coupling between disturbance compensation and delayed feedback, thereby reducing the admissible controller-gain region [17].

To improve time-varying disturbance estimation, Xu et al. [18] combined a nonlinear disturbance observer with predictive control, Zhao et al. [19] used an extended disturbance observer to estimate steering resistance torque and unmeasured states, and Ayati et al. [20] employed a fast disturbance observer to compensate for uncertainty, external disturbances, and input saturation. High-order observers can improve the tracking of rapidly varying disturbances by estimating their derivatives [21]. However, when combined with predictive, sliding-mode, or prescribed-performance control, their results reflect overall composite-system performance. Higher-order estimation also requires sufficient signal smoothness, while faster observer dynamics may amplify noise and neglected plant dynamics [22,23]. Improved disturbance tracking therefore does not necessarily enlarge the delay-dependent stability region.

Other studies have focused on improving closed-loop stability characteristics. Jeong et al. [24] switched the nominal model and adjusted the filter for different operating conditions, while Chang et al. [25] introduced an embedded filter to reshape the compensation channel. Filter designs have also been developed for communication delays, multivariable time-delay plants, and nonminimum-phase systems [26–28]. However, these methods often rely on a lower filter cutoff frequency or weaker compensation, potentially slowing the disturbance response. Maintaining time-varying disturbance tracking while enlarging the stability region therefore remains challenging.

Higher-order disturbance estimation and filter-embedded disturbance observers have been studied previously. This work applies compensation shaping to a time-delayed corner module steering system and evaluates its effect on sampled-data stability. The shaping filter acts on the estimated torque downstream of the observer, allowing the compensation dynamics to be adjusted while retaining the nominal observer poles. Section 2 establishes the delay-affected corner module model and baseline PD feedforward control system. Section 3 presents the conventional DOb and Shaped DOb. Section 4 derives the delay-dependent characteristic equations and determines the stability boundaries using D-curves. Section 5 compares the closed-loop stability regions and rightmost characteristic roots and evaluates steering-angle tracking and disturbance estimation. Section 6 summarizes the conclusions.

2. Steering System Model of the Single Corner Module

Distributed steer-by-wire vehicles remove the mechanical constraints imposed on individual wheel angles by conventional steering linkages. Each corner module independently tracks the target angle assigned by the high-level controller [29]. This architecture increases the flexibility of yaw control and tire lateral force allocation but makes coordinated steering dependent on the dynamic response of each module. A model incorporating the steering motor, reduction mechanism, wheel-end inertia, and equivalent damping is therefore required for controller and disturbance observer design [17].

Figure 1 shows the mechanical configuration of a corner module and the main torques acting about its steering axis. Besides the motor control torque, the actuator is affected by tire self-aligning torque, friction, unmodeled compliance, and parameter uncertainties. These effects are represented by a lumped disturbance torque $\mathrm{Td}(\mathrm{t})$, and the equivalent dynamics are expressed as:

$$J_{\mathrm{w}}\ddot{\theta}(t) + C_{\mathrm{w}}\dot{\theta}(t) + K_{\mathrm{w}}\theta(t) = T_{\mathrm{SM}}(t) + T_{\mathrm{d}}(t), \tag{1}$$

where $\theta(t)$ is the actual wheel steering angle; J_w, C_w, and K_w are the equivalent rotational inertia, viscous damping, and torsional stiffness referred to the steering axis; and $T_{SM}(t)$ is the motor torque transmitted through the reduction mechanism. The nominal second-order model uses fixed equivalent parameters J_w, C_w, and K_w to examine compensation–delay coupling.

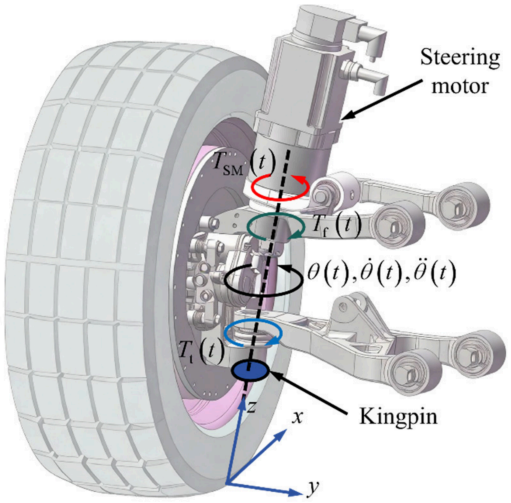


Figure 1. Mechanical configuration of the steering corner module.

The lumped disturbance torque comprises tire self-aligning torque, mechanical friction, road impacts, load transfer, and unmodeled compliance. During successive lane changes, emergency steering, or abrupt adhesion changes, these loads may excite the inertial and elastic dynamics of the corner module, causing transient wheel-angle oscillations.

In the baseline control system without a DOb, the control torque consists of a nominal model feedforward term and a delayed PD feedback term:

$$T_{SM}(t) = J_w\ddot{\theta}_d(t) + C_w\dot{\theta}_d(t) + K_w\theta_d(t) + K_P[\theta_d(t) - \theta(t-\tau)] + K_D[\dot{\theta}_d(t) - \dot{\theta}(t-\tau)], \quad (2)$$

where $\theta_d(t)$ is the desired wheel steering angle and τ is the equivalent feedback delay. The first three terms form the nominal model feedforward component, compensating for the inertia, damping, and stiffness torques required by the reference trajectory. The remaining terms form the delayed PD feedback component. τ denotes feedback latency under ideal torque actuation. Actuator lag or input delay affects the entire torque command, including feedforward and compensation, and requires separate modeling.

As indicated by the control law, the feedback delay affects only the actual steering angle and angular velocity. It does not alter the nominal model feedforward term, but changes both the closed-loop characteristic equation and the transfer relationship between the reference input and the actual steering angle.

Under zero initial conditions, $\Theta(s)$ and $\Theta_d(s)$ denote the Laplace transforms of $\theta(t)$ and $\theta_d(t)$, respectively. Neglecting external disturbances, the closed-loop transfer function is obtained as [30]:

$$\frac{\Theta(s)}{\Theta_d(s)} = \frac{J_w s^2 + (C_w + K_D)s + K_w + K_P}{J_w s^2 + C_w s + K_w + (K_D s + K_P)e^{-s\tau}}. \quad (3)$$

This relationship describes the wheel-angle response determined by the steering actuator and delayed feedback. When $\tau = 0$ and the nominal model is accurate, the numerator and denominator are identical, yielding ideal unit-gain tracking. When $\tau > 0$, the delay term breaks this equivalence and causes tracking error even without external disturbances.

Defining the tracking error as $E(s) = \Theta_d(s) - \Theta(s)$, the transfer relationship from the reference input to the tracking error is:

$$\frac{E(s)}{\Theta_d(s)} = \frac{(K_D s + K_P)(e^{-s\tau} - 1)}{J_w s^2 + C_w s + K_w + (K_D s + K_P)e^{-s\tau}}. \quad (4)$$

Feedback delay affects both closed-loop stability and nominal tracking accuracy. Different DOb configurations must therefore be compared using the same delay, reference signal, and PD gains. Since stability depends only on the homogeneous dynamics, setting $\theta_d(t) = 0$ and $T_d(t) = 0$ gives the baseline characteristic equation without a DOb:

$$J_w s^2 + C_w s + K_w + (K_D s + K_P)e^{-s\tau} = 0. \quad (5)$$

3. Disturbance Observer Design

Steering corner modules experience external disturbances and parameter variations. Higher PD gains can improve disturbance rejection but reduce stability under feedback delay. The conventional DOb serves as a benchmark, while the Shaped DOb estimates disturbance torque and its rate and filters the compensation output. Let $u_o(t)$ denote the observer torque input.

3.1. Conventional DOb Design

The conventional DOb reconstructs the lumped disturbance torque using the nominal steering model, known control input, and delayed state measurements, as shown in Figure 2.

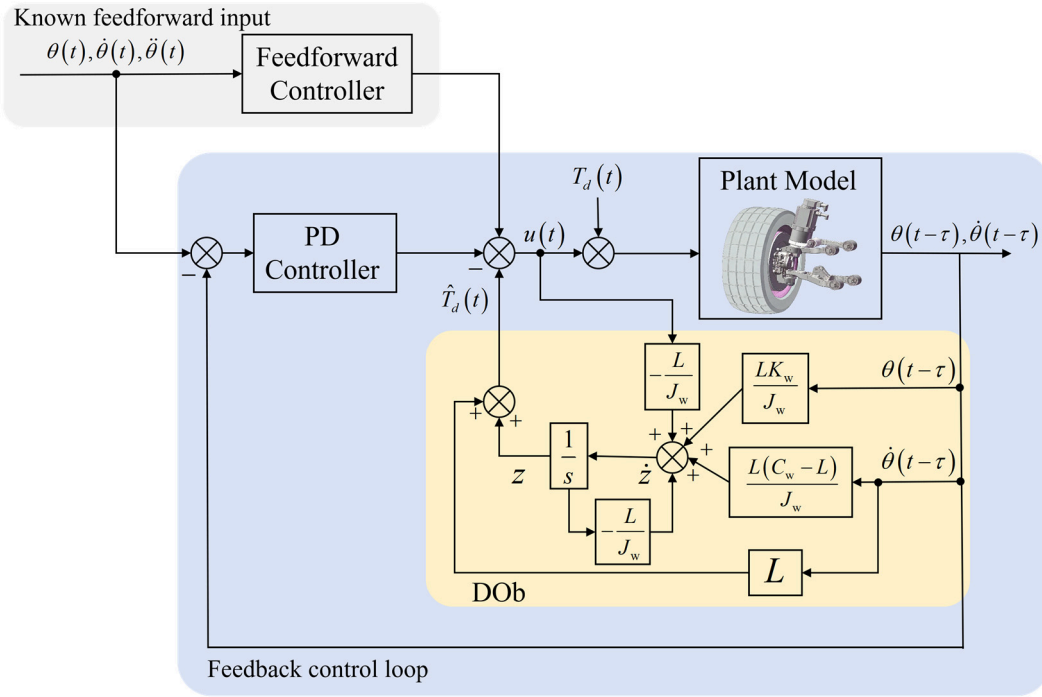


Figure 2. Closed-loop control structure using a DOb.

Let v(t) denote the feedforward and PD torque given by the right-hand side of Equation (2). With disturbance compensation, the applied motor torque is:

$$u(t) = T_{SM}(t) = v(t) - T_{comp}(t). \quad (6)$$

where $T_{comp}(t)$ is the compensation torque, equal to the disturbance estimate for the conventional DOb, and $u_o(t)$ denotes the observer torque input. The current-input implementation uses $u_o(t) = u(t)$, whereas the aligned-input implementation uses $u_o(t) = u(t - \tau)$.

Define the delayed states as $\theta_\tau(t) = \theta(t-\tau)$ and $\theta_{\dot\tau}(t) = \dot\theta(t-\tau)$, respectively. With observer state $z(t)$ and observer gain $L(>0)$, the disturbance estimate is expressed as:

$$\hat{T}_\mathrm{d}(t) = z(t) + L\dot\theta_\tau(t). \tag{7}$$

The dynamics of the corresponding internal torque state are expressed as:

$$\dot z(t) = -\frac{L}{J_\mathrm{w}} z(t) + \frac{L(C_\mathrm{w} - L)}{J_\mathrm{w}}\dot\theta_\tau(t) + \frac{LK_\mathrm{w}}{J_\mathrm{w}}\theta_\tau(t) - \frac{L}{J_\mathrm{w}}u_\mathrm{o}(t). \tag{8}$$

3.2. Shaped DOb Design

The conventional DOb estimates disturbance torque from the current model residual and therefore lags under rapidly varying wheel-end loads. The Shaped DOb additionally estimates the disturbance rate and uses the load trend to correct the compensation torque, making it more suitable for lane changes, emergency steering, and abrupt adhesion changes. It uses the available steering angle, angular velocity, and motor input without an additional torque sensor.

Figure 3 shows the Shaped DOb integrated with the same actuator, feedforward controller, and PD feedback loop. Under nominal conditions with time-aligned delayed measurements and control input, the disturbance torque and rate estimation errors relative to $T_\mathrm{d}(t-\tau)$ converge to zero for locally affine disturbances [31]. For general time-varying disturbances, bounded disturbance derivatives yield bounded estimation errors, as derived in Appendix A.

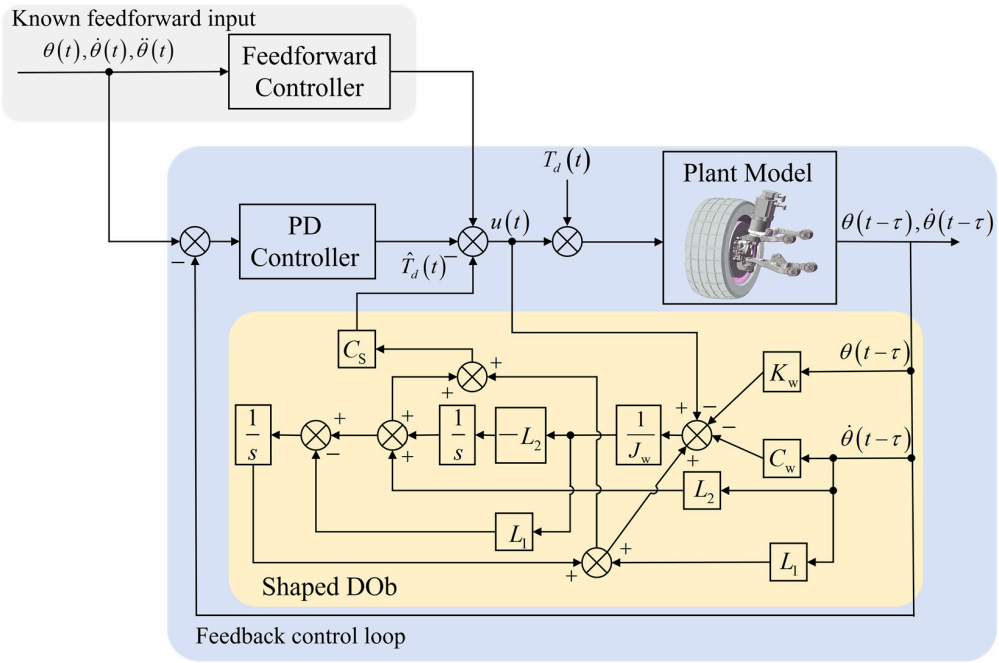


Figure 3. Closed-loop control structure using a Shaped DOb.

Introducing the internal observer states $p_1(t)$ and $p_2(t)$, the disturbance torque and its rate are estimated as follows:

$$\begin{cases} \hat T_\mathrm{d}(t) = p_1(t) + L_1\dot\theta_\tau(t) \\ \hat{\dot T}_\mathrm{d}(t) = p_2(t) + L_2\dot\theta_\tau(t). \end{cases} \tag{9}$$

where $L_1 > 0$ and $L_2 > 0$ are the observer gains of the Shaped DOb.

The internal-state dynamics of the Shaped DOb are then expressed as:

$$\begin{cases} \dot{p}_1(t) = \hat{\dot{T}}_d(t) - L_1 r_S(t) \\ \dot{p}_2(t) = -L_2 r_S(t). \end{cases} \tag{10}$$

where the first state equation predicts the disturbance torque from its estimated rate, and the second corrects the rate estimate using the model residual. This enables the Shaped DOb to track time-varying disturbances faster than the conventional DOb.

Under nominal conditions, the transfer relationship from the delayed disturbance to its estimate is:

$$\begin{aligned} Q_H(s) &= \frac{\hat{T}_d(s)}{D_\tau(s)} = \frac{L_1 s + L_2}{J_w s^2 + L_1 s + L_2} \\ D_\tau(s) &= e^{-s\tau} \cdot T_d(s). \end{aligned} \tag{11}$$

Appendix A presents the Shaped DOb error convergence and gain design. Compared with the conventional DOb, $Q_H(s)$ includes disturbance rate dynamics, reducing phase lag at low and medium frequencies and improving wheel-end torque tracking.

Higher Shaped DOb gains accelerate estimation but may introduce excessive high-frequency content into the motor command. A shaping filter is therefore used to preserve compensation in the main steering frequency range while limiting torque variations beyond the actuator response range [32]:

$$C_S(s) = \frac{T_z s + 1}{\left(T_{p1} s + 1\right)\left(T_{p2} s + 1\right)}. \tag{12}$$

The shaping filter time constants are $T_z = 0.010$ s, $T_{p1} = 0.600$ s, and $T_{p2} = 0.040$ s, corresponding to pole frequencies of 0.265 and 3.979 Hz and a zero frequency of 15.915 Hz. At the reference setting $L = 50$, the dominant filter pole lies below the nominal observer pole frequency of 1.224 Hz, and T_{p2} is set equal to the reference feedback delay of 0.04 s. The second pole, set by T_{p2}, adds attenuation and phase lag at higher frequencies. The zero, set by T_z, moderates the attenuation and partially offsets the phase lag introduced by the poles.

The zero frequency, pole natural frequency, and damping ratio of the shaping filter are defined as $\omega_z = 1/T_z$, $\omega_s = 1/\sqrt{(T_{P1} T_{P2})}$ $(\omega_s > 0)$, $\zeta_s = (T_{P1} + T_{P2})/(2\sqrt{(T_{P1} T_{P2})})$ $(\zeta_s \geq 1)$, respectively. The shaping filter can then be equivalently expressed as:

$$C_s(s) = \frac{1 + s/\omega_z}{s^2/\omega_s^2 + 2\zeta_s s/\omega_s + 1}. \tag{13}$$

Matching the corresponding coefficients gives:

$$T_z = \frac{1}{\omega_z},\ T_{p1,p2} = \frac{\zeta_s \pm \sqrt{\zeta_s^2 - 1}}{\omega_s}. \tag{14}$$

The filter acts on the compensation output, while Q_H retains its nominal estimation dynamics. Increasing T_{p1} narrows the compensation bandwidth and strengthens noise attenuation. T_{p2} mainly controls higher-frequency attenuation, whereas increasing T_Z reduces phase lag at the expense of greater high-frequency gain. These trade-offs are quantified in Section 5.1.

The shaped compensation torque is:

$$T_{comp}(t) = q_1(t) + T_z q_2(t). \tag{15}$$

The nominal equivalent compensation kernel of the Shaped DOb is:

$$Q_{SH}(s) = C_S(s) Q_H(s) = \frac{(T_z s + 1)(L_1 s + L_2)}{\left(T_{p1} s + 1\right)\left(T_{p2} s + 1\right)(J_w s^2 + L_1 s + L_2)}. \tag{16}$$

For additive angle and angular velocity measurement noise with Laplace transforms N_θ and N_v, direct propagation through the nominal observer and shaping channels gives:

$$\begin{aligned} \hat{T}_{d,n}(s) &= Q_H(s)[K_w N_\theta(s) + (J_w s + C_w)N_v(s)] \\ T_{\mathrm{comp},n}(s) &= C_s(s)\hat{T}_{d,n}(s). \end{aligned} \tag{17}$$

Thus, shaping attenuates the noise transmitted to the compensation output. Its effects on compensation bandwidth and phase are evaluated separately from raw disturbance estimation accuracy.

4. Stability Analysis

A distributed steer-by-wire corner module must remain stable as vehicle speed, tire load, and communication delay vary; otherwise, steering angle oscillations may affect lateral force allocation and yaw control. The D-curve method maps the critical stability conditions onto the K_P–K_D plane [17]. The stability region area quantifies the extent of admissible controller gains under feedback delay and provides a basis for comparing controller-tuning flexibility.

4.1. Steering Control System with the Conventional DOb

Substituting the conventional DOb compensation torque into the delayed corner module dynamics produces state terms at $t-\tau$ and $t-2\tau$ because both the observer measurements and control input contain delayed feedback [33]. The first term represents one passage through the feedback channel, while the second results from the delayed states passing through the observation and compensation channel again. Thus, $t-2\tau$ is a composite feedback delay rather than an additional physical delay.

The disturbance estimation error dynamics follow from the conventional DOb state equation [34]:

$$\dot{e}_d(t) = \dot{T}_d(t) - \frac{L}{J_w}\big[K_P\theta(t-\tau) + K_D\dot{\theta}(t-\tau)\big] + \frac{L}{J_w}\big[K_P\theta(t-2\tau) + K_D\dot{\theta}(t-2\tau)\big] - \frac{L}{J_w}e_d(t-\tau), \tag{18}$$

where the conventional DOb introduces delayed terms at both $t-\tau$ and $t-2\tau$, with the latter originating from the delayed control input $T_{\mathrm{SM}}(t-\tau)$.

Equation (17) shows that the conventional DOb changes the equivalent damping and disturbance compensation characteristics and couples the PD gains with the delayed states through L. For characteristic root computation, an augmented state vector containing the wheel angle, angular velocity, and disturbance estimation error is introduced:

$$\tilde{\mathbf{x}}_{\mathrm{D}}(t) = \begin{bmatrix} \dot{\tilde{\theta}}(t) & \tilde{\theta}(t) & e_{\mathrm{d}}(t) \end{bmatrix}^{\mathrm{T}}. \tag{19}$$

The closed-loop system with the conventional DOb is expressed as:

$$\dot{\tilde{\mathbf{x}}}_{\mathrm{D}}(t) = \mathbf{A}_{\mathrm{D}}\tilde{\mathbf{x}}_{\mathrm{D}}(t) + \mathbf{B}_{\mathrm{D},1}\tilde{\mathbf{x}}_{\mathrm{D}}(t-\tau) + \mathbf{B}_{\mathrm{D},2}\tilde{\mathbf{x}}_{\mathrm{D}}(t-2\tau), \tag{20}$$

where the coefficient matrices are $\mathbf{A}_{\mathrm{D}} = \begin{bmatrix} -\frac{C_{\mathrm{w}}}{J_{\mathrm{w}}} & -\frac{K_{\mathrm{w}}}{J_{\mathrm{w}}} & \frac{1}{J_{\mathrm{w}}} \\ 1 & 0 & 0 \\ 0 & 0 & 0 \end{bmatrix}$, $\mathbf{B}_{\mathrm{D},1} = \begin{bmatrix} -\frac{K_{\mathrm{D}}}{J_{\mathrm{w}}} & -\frac{K_{\mathrm{P}}}{J_{\mathrm{w}}} & 0 \\ 0 & 0 & 0 \\ -\frac{LK_{\mathrm{D}}}{J_{\mathrm{w}}} & -\frac{LK_{\mathrm{P}}}{J_{\mathrm{w}}} & -\frac{L}{J_{\mathrm{w}}} \end{bmatrix}$, $\mathbf{B}_{\mathrm{D},2} = \begin{bmatrix} 0 & 0 & 0 \\ 0 & 0 & 0 \\ \frac{LK_{\mathrm{D}}}{J_{\mathrm{w}}} & \frac{LK_{\mathrm{P}}}{J_{\mathrm{w}}} & 0 \end{bmatrix}$.

Assuming an exponential solution of the form $\tilde{\mathrm{x}}_{\mathrm{D}}(t) = \mathrm{c}_{\mathrm{D}}e^{\lambda t}$ for the augmented system [35], the characteristic determinant of the closed-loop system with the conventional DOb is obtained as:

$$\Delta_{\mathrm{D}}(\lambda) = \det\big[\lambda\mathbf{I}_3 - \mathbf{A}_{\mathrm{D}} - \mathbf{B}_{\mathrm{D},1}e^{-\lambda\tau} - \mathbf{B}_{\mathrm{D},2}e^{-2\lambda\tau}\big] = 0. \tag{21}$$

On the dynamic stability boundary, the characteristic root is set to $\lambda = \mathrm{i}\omega(\omega > 0)$. Define $c_1 = \cos(\omega\tau)$, $s_1 = \sin(\omega\tau)$, $L = L/J_w$, $a(\omega) = K_w/J_w\text{-}\omega^2$, $b(\omega) = C_w\cdot\omega/J_w$.

To obtain the D-curve in the K_P–K_D plane, the characteristic determinant is separated into real and imaginary parts. Expanding the delay terms gives two affine equations in K_P and K_D.

The determinant of the conventional DOb is written as:

$$\Delta_D(\mathrm{i}\omega) = d_{0,D} + d_{P,D}K_P + d_{D,D}K_D. \tag{22}$$

The real and imaginary parts of the characteristic determinant for the conventional DOb are expressed as:

$$\begin{aligned} R_D(\omega) &= r_{0,D} + r_{P,D}K_P + r_{D,D}K_D \\ S_D(\omega) &= s_{0,D} + s_{P,D}K_P + s_{D,D.}K_D \end{aligned} \tag{23}$$

Setting both parts equal to zero yields:

$$\begin{bmatrix} r_{P,D} & r_{D,D} \\ s_{P,D} & s_{D,D} \end{bmatrix} \begin{bmatrix} K_P \\ K_D \end{bmatrix} + \begin{bmatrix} r_{0,D} \\ s_{0,D} \end{bmatrix} = \mathbf{0}. \tag{24}$$

Provided that $\mathrm{d}_{P,R}\mathrm{d}_{D,I} - \mathrm{d}_{D,R}\mathrm{d}_{P,I} \neq 0$, the dynamic stability boundary of the conventional DOb is obtained as:

$$\begin{bmatrix} K_{P,D}(\omega) \\ K_{D,D}(\omega) \end{bmatrix} = -\begin{bmatrix} r_{P,D} & r_{D,D} \\ s_{P,D} & s_{D,D} \end{bmatrix}^{-1} \begin{bmatrix} r_{0,D} \\ s_{0,D} \end{bmatrix}. \tag{25}$$

For a fixed observer gain $\mathrm{L} > 0$, expansion of the characteristic equation in Appendix B about $\lambda = 0$ shows that the delay-dependent correction starts at second order in λ. The low-frequency limit is therefore:

$$\begin{cases} K_P(0) = -K_w \\ K_D(0) = -C_w. \end{cases} \tag{26}$$

Solving these equations over ω produces the conventional DOb D-curve. Each point gives a K_P and K_D pair corresponding to sustained wheel-angle oscillation. Characteristic roots at representative points identify the stable side, while crossing the boundary may cause instability.

The corner module parameters used for all observer configurations are listed in Table 1.

Table 1. Model parameters of the steering system.

Parameters	Value	Unit
J_w	6.5	kg·m^2
C_w	35	N·m·s/rad
K_w	8000	N·m/rad

Throughout this paper, K_P and L_2 are expressed in N·m/rad, whereas K_D, L, and L_1 are expressed in N·m·s/rad.

Figure 4 shows the effects of observer gain and feedback delay on the stability region of the conventional DOb. The red dashed line is the static boundary $K_P = -K_w$, with the static unstable region to its left. The region between this line and the blue dynamic boundary, verified by characteristic roots, is stable. Darker curves indicate larger delay or observer gain. The characteristic equations are formulated in continuous time.

The left panel fixes $L = 50$. At $\tau = 0$, the dynamic boundary becomes $K_D = -C_w$ and the stability region is largest. As τ increases from 0.02 to 0.10 s, the boundary curves inward and contracts. The right panel fixes $\tau = 0.02$ s. Increasing L from 0.1 to 50 also shrinks the stability

region. Although a larger L increases the estimation bandwidth, it strengthens the coupling between compensation and delay, increasing phase loss and reducing the stability margin.

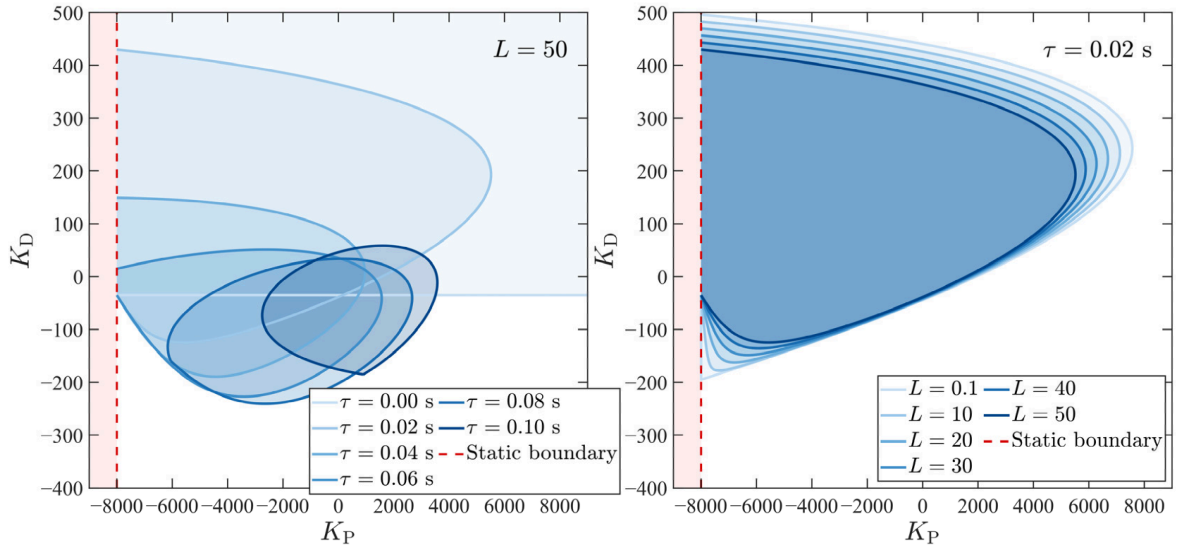


Figure 4. Influence of delay and observer gain on conventional DOb stability.

Together, the panels show that increasing the conventional DOb gain accelerates disturbance estimation but shrinks the stability region under feedback delay.

4.2. Steering Control System with the Shaped DOb

The Shaped DOb adds disturbance rate estimation and shaping filter states, increasing the closed-loop order [25]. To remove the constant disturbance operating point from the homogeneous model, denote the equilibrium torque by T_{d0} and define the filter deviation states as:

$$\begin{cases} \bar{q}_1(t) = q_1(t) - T_{d0} \\ \bar{q}_2(t) = q_2(t). \end{cases} \tag{27}$$

For the homogeneous stability analysis, $\dot{T}_{d0} = 0$, $\ddot{T}_{d0} = 0$. The deviation states then satisfy:

$$\begin{cases} \dot{\bar{q}}_1(t) = \bar{q}_2(t), \\ \dot{\bar{q}}_2(t) = \frac{-e_1(t) - \bar{q}_1(t) - (T_{p1} + T_{p2})\bar{q}_2(t)}{T_{p1} T_{p2}}. \end{cases} \tag{28}$$

The Shaped DOb model includes the steering, disturbance estimation, and compensation torque dynamics. Expressing the filter in deviation form driven by the estimation error removes the constant load operating point. An augmented state model then determines the boundary between decaying and sustained oscillations under different controller gains:

$$\mathbf{x}_{SH}(t) = \begin{bmatrix} \dot{\theta}(t) & \theta(t) & e_1(t) & e_2(t) & \bar{q}_1(t) & \bar{q}_2(t) \end{bmatrix}^T. \tag{29}$$

where e_1 and e_2 denote the disturbance torque and disturbance rate estimation errors, respectively, as defined in Appendix A.

The closed-loop system with the Shaped DOb is then expressed as:

$$\dot{\tilde{\mathbf{x}}}_{SH}(t) = \mathbf{A}_{SH}\tilde{\mathbf{x}}_{SH}(t) + \mathbf{B}_{SH,1}\tilde{\mathbf{x}}_{SH}(t-\tau) + \mathbf{B}_{SH,2}\tilde{\mathbf{x}}_{SH}(t-2\tau), \tag{30}$$

where the coefficient matrices are: $\mathbf{A}_{\mathrm{SH}} = \begin{bmatrix} -\frac{C_w}{J_w} & -\frac{K_w}{J_w} & 0 & 0 & -\frac{1}{J_w} & -\frac{T_z}{J_w} \\ 1 & 0 & 0 & 0 & 0 & 0 \\ 0 & 0 & -\frac{L_1}{J_w} & 1 & -\frac{L_1}{J_w} & -\frac{L_1 T_z}{J_w} \\ 0 & 0 & -\frac{L_2}{J_w} & 0 & -\frac{L_2}{J_w} & -\frac{L_2 T_z}{J_w} \\ 0 & 0 & 0 & 0 & 0 & 1 \\ 0 & 0 & -\frac{1}{T_{p1}T_{p2}} & 0 & -\frac{1}{T_{p1}T_{p2}} & -\frac{T_{p1}+T_{p2}}{T_{p1}T_{p2}} \end{bmatrix}$,

$\mathbf{B}_{\mathrm{SH},1} = \begin{bmatrix} -\frac{K_D}{J_w} & -\frac{K_P}{J_w} & 0 & 0 & 0 & 0 \\ 0 & 0 & 0 & 0 & 0 & 0 \\ -\frac{L_1 K_D}{J_w} & -\frac{L_1 K_P}{J_w} & 0 & 0 & \frac{L_1}{J_w} & \frac{L_1 T_z}{J_w} \\ -\frac{L_2 K_D}{J_w} & -\frac{L_2 K_P}{J_w} & 0 & 0 & \frac{L_2}{J_w} & \frac{L_2 T_z}{J_w} \\ 0 & 0 & 0 & 0 & 0 & 0 \\ 0 & 0 & 0 & 0 & 0 & 0 \end{bmatrix}$, $\mathbf{B}_{\mathrm{SH},2} = \begin{bmatrix} 0 & 0 & 0 & 0 & 0 & 0 \\ 0 & 0 & 0 & 0 & 0 & 0 \\ \frac{L_1 K_D}{J_w} & \frac{L_1 K_P}{J_w} & 0 & 0 & 0 & 0 \\ \frac{L_2 K_D}{J_w} & \frac{L_2 K_P}{J_w} & 0 & 0 & 0 & 0 \\ 0 & 0 & 0 & 0 & 0 & 0 \\ 0 & 0 & 0 & 0 & 0 & 0 \end{bmatrix}$.

Setting $\mathrm{s} = \mathrm{i}\omega$ and separating the determinant into real and imaginary parts gives a linear system in K_P and K_D because both gains remain affine in the characteristic equation:

$$\Delta_{\mathrm{SH}}(\lambda) = \det\left[\lambda \mathbf{I}_6 - \mathbf{A}_{\mathrm{SH}} - \mathbf{B}_{\mathrm{SH},1} e^{-\lambda\tau} - \mathbf{B}_{\mathrm{SH},2} e^{-2\lambda\tau}\right] = 0. \tag{31}$$

Similarly, setting $\lambda = \mathrm{i}\omega$, with $\omega > 0$, on the dynamic stability boundary gives:

$$\Delta_{\mathrm{SH}}(\mathrm{i}\omega) = R_{\mathrm{SH}}(\omega) + \mathrm{i} S_{\mathrm{SH}}(\omega) = 0. \tag{32}$$

Therefore, the following expression is obtained:

$$\begin{cases} R_{\mathrm{SH}}(\omega) = r_{0,\mathrm{SH}} + r_{\mathrm{P,SH}} K_P + r_{\mathrm{D,SH}} K_D \\ S_{\mathrm{SH}}(\omega) = s_{0,\mathrm{SH}} + s_{\mathrm{P,SH}} K_P + s_{\mathrm{D,SH}} K_D. \end{cases} \tag{33}$$

The dynamic stability boundary satisfies:

$$\begin{bmatrix} r_{\mathrm{P,SH}} & r_{\mathrm{D,SH}} \\ s_{\mathrm{P,SH}} & s_{\mathrm{D,SH}} \end{bmatrix} \begin{bmatrix} K_P \\ K_D \end{bmatrix} + \begin{bmatrix} r_{0,\mathrm{SH}} \\ s_{0,\mathrm{SH}} \end{bmatrix} = \mathbf{0}. \tag{34}$$

When the Jacobian matrix is nonsingular, the dynamic stability boundary of the Shaped DOb is expressed as:

$$\begin{bmatrix} K_{\mathrm{P,SH}}(\omega) \\ K_{\mathrm{D,SH}}(\omega) \end{bmatrix} = -\begin{bmatrix} r_{\mathrm{P,SH}} & r_{\mathrm{D,SH}} \\ s_{\mathrm{P,SH}} & s_{\mathrm{D,SH}} \end{bmatrix}^{-1} \begin{bmatrix} r_{0,\mathrm{SH}} \\ s_{0,\mathrm{SH}} \end{bmatrix}. \tag{35}$$

Equations (19) and (29) are continuous-time models. Figures 4–6 combine continuous mechanical and PD terms at $s = i\omega$ with discrete observer kernels at $z = \exp(i\omega T_s)$, where $T_s = 5$ ms. Both kernels use forward-Euler reference poles, with an additional backward-difference term in the higher-order kernel. The shaping filter uses Tustin discretization. For $\tau = N\,T_s$, the delay satisfies $\exp(-i\omega\tau) = z^{-N}$.

In Section 5, exact integration with held feedback and integer-sample delays yields the augmented state-transition matrix. Sampled-data stability requires all its eigenvalues to lie inside the unit circle. The resulting limits are compared with the corresponding continuous-time limits.

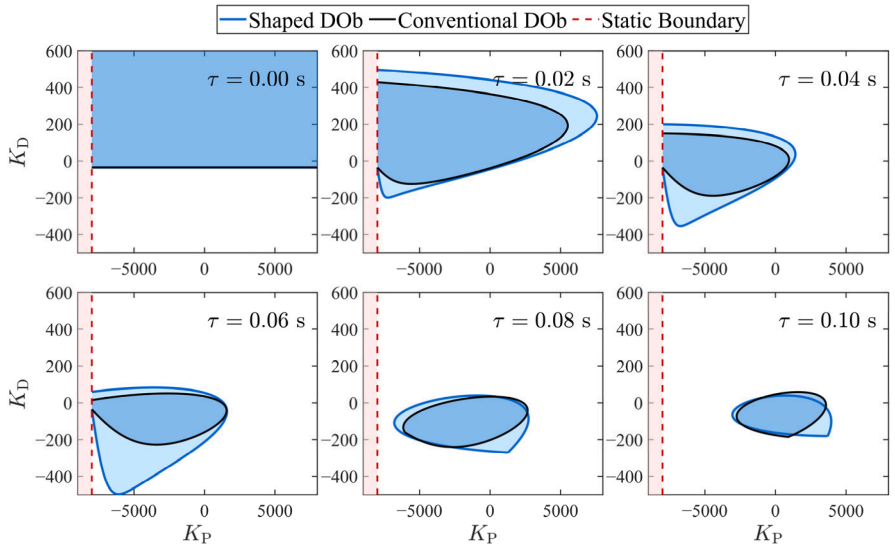


Figure 5. Stability regions of two DObs under different time delays.

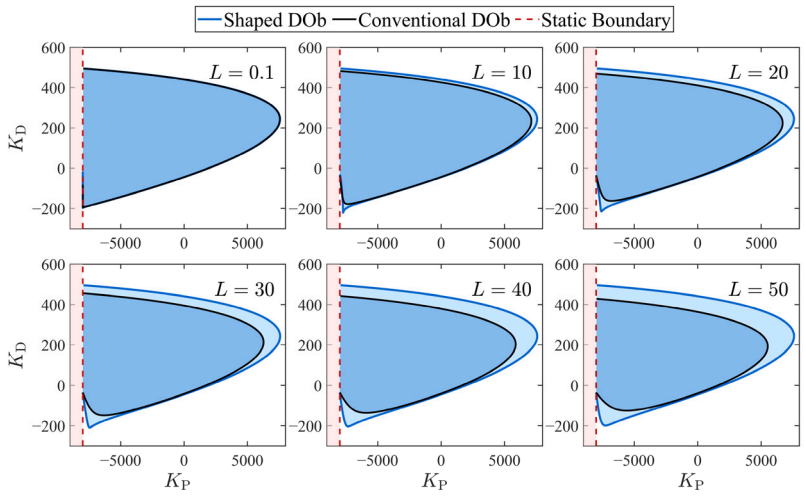


Figure 6. Stability regions of two DObs under different observer gains.

5. Results and Discussion

This section focuses on the stability region expansion achieved by the Shaped DOb while maintaining comparable steering-angle tracking accuracy. Stability regions are compared under different feedback delays and reference observer gains, and the corresponding boundaries are examined through characteristic root analysis. Practical relevance is assessed using physically meaningful positive PD gains and stability margins at representative controller settings. Time-domain responses obtained with the parameters of the stability region analysis are also compared.

5.1. Comparison of Stability Regions

With the reference observer gain fixed at $L = 50$, D-curves are generated for both observers at $\tau = 0$, 0.02, 0.04, 0.06, 0.08, and 0.10 s. In Figure 5, the red dashed line is the static boundary $K_P = -K_w$ at s = 0, while the black and blue curves are the dynamic boundaries of the conventional DOb and Shaped DOb. The shaded areas are the stability regions verified by characteristic roots.

For the nominal continuous-time model at zero delay, the effective stiffness and damping are $K_w + K_P$ and $C_w + K_D$. Negative proportional and derivative gains reduce the

restoring torque and damping, respectively, but may remain mathematically stable because of the mechanical stiffness and damping. These regions describe the complete stability domain; practical comparisons below use positive PD gains.

At $\tau = 0$, the two boundaries nearly coincide. As τ increases, they contract into smaller closed regions, restricting the admissible ranges of K_P and K_D. The Shaped DOb boundary lies outside the conventional DOb boundary over most of the parameter plane and provides a larger stability region. The area ratio is defined as:

$$\eta_A = \frac{A_{\text{Shaped}}}{A_{\text{DOb}}}. \tag{36}$$

At $\tau = 0.02$, 0.04, 0.06, 0.08, and 0.10 s, the area ratios η_A are 1.329, 1.528, 1.914, 1.282, and 1.083, respectively. The largest expansion occurs at $\tau = 0.06$ s, where the Shaped DOb region is 1.91 times that of the conventional DOb. At $\tau = 0.10$ s, the boundaries intersect and neither region strictly contains the other, but the net stability area still increases by 8.3%. Thus, the proposed method retains a wider controller parameter range as the delay increases.

With τ fixed at 0.02 s, L is varied from 0.1 to 50 to examine its effect on stability. The shaping filter time constants were held fixed in the sweeps in Figures 5 and 6 at $T_z = 0.010$ s, $T_{p1} = 0.600$ s, and $T_{p2} = 0.040$ s. For each reference gain L, the nominal error pole of the conventional DOb at $-L/J_w$ was used as the repeated-pole target for the Shaped DOb, as described in Appendix A. At $L = 50$, this design gives $L_1 = 100$ and $L_2 = 384.6154$.

At $L = 0.1$, the boundaries nearly coincide because the low observer bandwidth weakens the compensation and shaping effects. As L increases, disturbance estimation becomes faster, but coupling between the conventional DOb and the delay strengthens, reducing its stability region from about 7.20×10^6 to 5.44×10^6, or 24.4%.

In contrast, the Shaped DOb stability region remains near 7.20×10^6 and is less sensitive to L. For $L = 0.1$, 10, 20, 30, 40, and 50, the area ratios η_A are 1.000, 1.052, 1.112, 1.179, 1.252, and 1.329. Its advantage therefore increases with L, reaching 32.9% at $L = 50$.

Varying τ at fixed L evaluates delay tolerance, while varying L at fixed τ evaluates sensitivity to observer bandwidth. The results show that the Shaped DOb limits stability region contraction and widens the feasible range for coordinated controller and observer design.

Figure 7 compares the two observers at a feedback delay of 0.04 s, a sampling period of 5 ms, and PD gains of $K_P = 50$ and $K_D = 1.5$. The conventional DOb uses $L = 50$, while the Shaped DOb uses $L_1 = 100$ and $L_2 = 384.6154$, selected using the nominal error-pole assignment in Appendix A. Over 3.5–5 s, the steering-angle tracking RMSEs are 0.0484 and 0.0050 rad for the conventional and Shaped DObs, respectively. Over 0–3 s, the raw disturbance torque estimation RMSEs are 8.63 and 8.58 N·m. Relative to the disturbance RMS of 11.171 N·m over the same interval, these correspond to normalized estimation errors of 77.24% and 76.79%, respectively. These results indicate similar estimation performance, although substantial residual errors remain. The principal benefit is assessed through stability region expansion while maintaining comparable tracking performance. The conventional and shaped configurations use current and time-aligned delayed torque inputs, respectively; this comparison therefore includes input timing effects.

Additional tests used 10 N·m step, half-cosine-rise (0.05 s), and sinusoidal disturbances at 0.5, 1, 2, and 5 Hz. Plant and controller parameters, feedback delay, sampling period, and aligned torque input timing were identical; observer gains followed the common nominal pole reference. Errors were calculated against the current disturbance using raw observer outputs. Transient RMSE was evaluated over $1 \le t < 3$ s, and sinusoidal metrics over five steady-state cycles. Rise time denotes the 10–90% response time, and settling time uses a $\pm 2\%$ tolerance band.

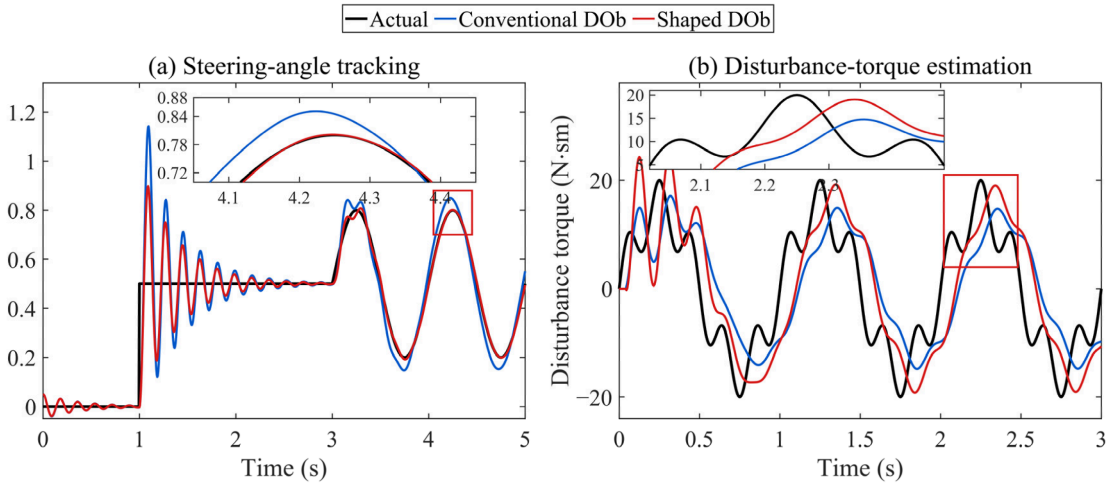


Figure 7. Time-domain comparison at a feedback delay of 0.04 s and a reference observer gain of 50. (**a**) Steering-angle tracking. (**b**) Disturbance torque estimation.

In Figure 8, the Shaped DOb reduces the step RMSE from 2.344 to 1.961 N·m and the rise time from 0.290 to 0.100 s, with 13.23% overshoot and an increased settling time from 0.545 to 0.780 s. For the rapid torque rise, RMSE decreases from 2.272 to 1.866 N·m.

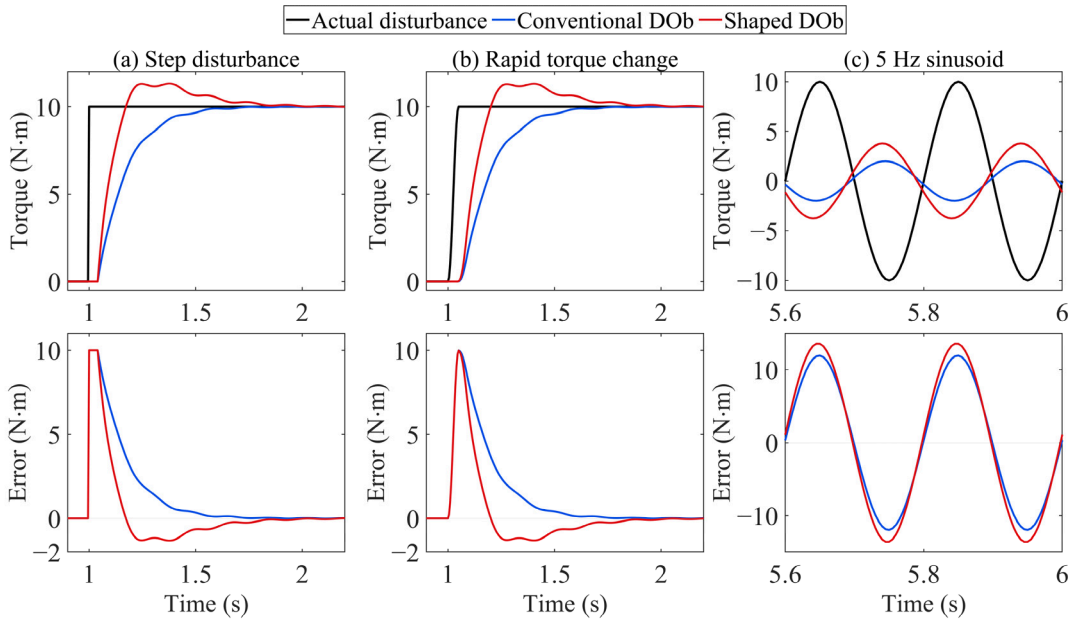


Figure 8. Disturbance torque estimates and estimation errors under (**a**) a step disturbance, (**b**) a rapid torque increase, and (**c**) a 5 Hz sinusoidal disturbance.

Table 2 compares the RMSE and phase lag of the raw disturbance estimates. The Unshaped DOb uses the same higher-order observer as the Shaped DOb, with the shaping filter bypassed. Compared with the conventional DOb, both higher-order configurations yield lower RMSE and smaller phase lag at 0.5 and 1 Hz. At 2 and 5 Hz, they retain smaller phase lag but yield higher RMSE. The largest differences between the Unshaped and Shaped DObs are 0.087 N·m in RMSE and 3.07° in phase lag, both at 5 Hz, indicating that compensation shaping has little effect on raw estimation under the tested conditions.

Four configurations (Conventional, Filtered, Unshaped, and Shaped DObs) use identical plant and controller parameters, time-aligned delayed torque inputs, and a common nominal pole reference. Bandwidth denotes the nominal −3 dB crossing relative to DC gain.

Independent Gaussian angle and velocity noise, with standard deviations of 0.001 rad and 0.01 rad/s, is held over each 5 ms sampling interval. Noise RMS is calculated over 10–60 s and averaged across ten realizations.

Table 2. Disturbance estimation RMSE (N·m) and phase lag (°) at different frequencies. Each cell lists RMSE/phase lag.

Frequency (Hz)	Conventional DOb	Unshaped DOb	Shaped DOb
0.5	3.598/30.33	1.882/13.31	1.880/13.30
1	6.011/55.51	4.833/36.27	4.822/36.20
2	8.043/91.27	8.489/77.03	8.468/76.74
5	8.461/169.56	9.558/159.57	9.645/162.64

The Filtered DOb retains the conventional first-order estimator and applies the following second-order filter to its raw disturbance estimate [25]:

$$F(s) = \frac{s^2 + 2\zeta_z \omega_f s + \omega_f^2}{s^2 + 2\zeta_p \omega_f s + \omega_f^2}. \tag{37}$$

where $\omega_f = 14$ rad/s, $\zeta_z = 0.35$, and $\zeta_p = 1.65$ define the empirical filter configuration used for the benchmark comparison.

Its disturbance-rejection performance, commanded-torque demand, and stability limits will be evaluated in the subsequent analyses to characterize the performance–stability trade-off.

Figure 9 excludes the common feedback delay. The conventional and higher-order observers have raw estimation bandwidths of 1.224 and 3.039 Hz, respectively. The compensation bandwidths are 0.542 Hz for the Filtered DOb and 0.289 Hz for the Shaped DOb. At 1 Hz, F and C_s add phase lags of 40.2° and 85.7°, respectively. The mean compensation-noise RMS values are 1.210, 0.888, 2.025, and 0.497 N·m for the Conventional, Filtered, Unshaped, and Shaped DObs, respectively.

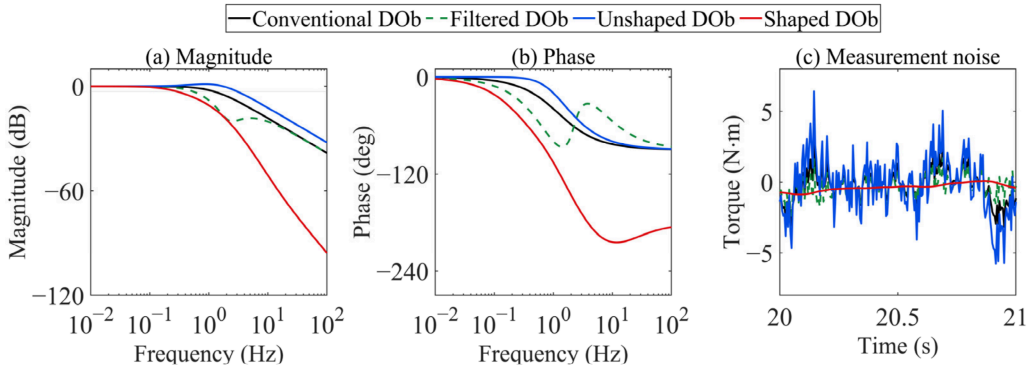


Figure 9. Frequency responses and measurement noise responses of four observer configurations.

The same noise settings and RMS evaluation procedure are used in Table 3. Table 3 summarizes the sensitivity of compensation bandwidth and noise RMS when each time constant is halved or doubled individually. Among the tested parameters, T_{p1} has the largest effect on both metrics. Increasing T_{p1} narrows the compensation bandwidth and reduces noise RMS. With T_z and T_{p2} held fixed, the adopted T_{p1} of 0.600 s yields a lower noise RMS than 0.300 s and a wider compensation bandwidth than 1.200 s.

Additional zero-reference tests used $T_d(t) = 15\sin(2\pi t) + 5\sin(10\pi t)$ N·m under nominal aligned-input settings. Table 4 summarizes the wheel-angle and commanded torque metrics over $5 \le t < 10$ s.

Table 3. Sensitivity of compensation bandwidth and noise RMS to shaping filter parameters.

T_z (ms)	T_{p1} (ms)	T_{p2} (ms)	Compensation Bandwidth (Hz)	Noise RMS (N·m)
10	600	40	0.2885	0.497
5	600	40	0.2884	0.497
20	600	40	0.2888	0.499
10	300	40	0.6561	0.700
10	1200	40	0.1356	0.341
10	600	20	0.2897	0.503
10	600	80	0.2839	0.483

Table 4. Wheel-angle RMS and commanded torque under a dual-frequency disturbance.

Configuration	Angle RMS (mrad)	Torque RMS (N·m)	Peak Torque (N·m)
w/o. DOb	2.2610	0.1421	0.2725
Conventional DOb	2.4691	8.2299	11.8961
Filtered DOb	2.4146	4.1723	6.2845
Unshaped DOb	2.6553	12.2296	18.9271
Shaped DOb	2.4113	2.9880	4.1250

Peak torque denotes the maximum absolute commanded torque. The Shaped and Filtered DObs yield similar angle RMS values of 2.4113 and 2.4146 mrad, respectively, while the Shaped DOb reduces commanded torque RMS from 4.1723 to 2.9880 N·m and peak torque from 6.2845 to 4.1250 N·m. This lower control effort is consistent with its narrower compensation bandwidth and stronger high-frequency attenuation in Figure 9, while comparable wheel-angle disturbance rejection is retained. Relative to the Unshaped DOb, shaping reduces angle RMS from 2.6553 to 2.4113 mrad and torque RMS from 12.2296 to 2.9880 N·m. The uncompensated system nevertheless has the lowest angle RMS of 2.2610 mrad because, for the tested 1 and 5 Hz disturbance components, phase lag in the compensation channel limits effective cancelation and can amplify the residual disturbance. This illustrates how disturbance rejection performance depends on the disturbance spectrum and the magnitude and phase of the complete compensation channel.

These results demonstrate that the Shaped DOb improves wheel-angle disturbance rejection relative to the Unshaped DOb and achieves comparable disturbance rejection to the Filtered DOb with substantially lower commanded torque demand under the tested conditions.

5.2. Comparison of Eigenvalue Characteristics

At $\tau = 0.02$ s, two parameter paths are selected to verify the D-curve boundaries using numerically computed rightmost characteristic roots. In Figure 10, the left panel shows the Shaped DOb boundary in blue, the conventional DOb boundary in black, and the static boundary as a red dashed line. In the right panels, dots and crosses represent the roots of the conventional DOb and Shaped DOb, while the black dashed line is the imaginary axis. Stability requires all rightmost roots to remain in the left half plane. Purple dots and red crosses mark unstable roots, and the enlarged views show their migration near the imaginary axis. In the characteristic root plots, $\mathrm{Re}(\lambda)$ and $\mathrm{Im}(\lambda)$ are expressed in s^{-1} and rad/s, respectively.

Characteristic roots were computed using multistart MATLAB fsolve with continuation, tolerances of 10^{-11}, and residuals below 10^{-6}. The search covered $-60 \le \mathrm{Re}(\lambda) \le 30\ \mathrm{s}^{-1}$ and $|\mathrm{Im}(\lambda)| \le 150$ rad/s. Stability was determined by the sign of the largest root real part.

At seven representative gain pairs, refining the initial guesses and expanding the search to $-100 \le \mathrm{Re}(\lambda) \le 100\ \mathrm{s}^{-1}$ and $|\mathrm{Im}(\lambda)| \le 600$ rad/s changed the largest real part by less than

10^{-8} s^{-1} and preserved all classifications. Contour winding confirmed the unstable-root counts within this window.

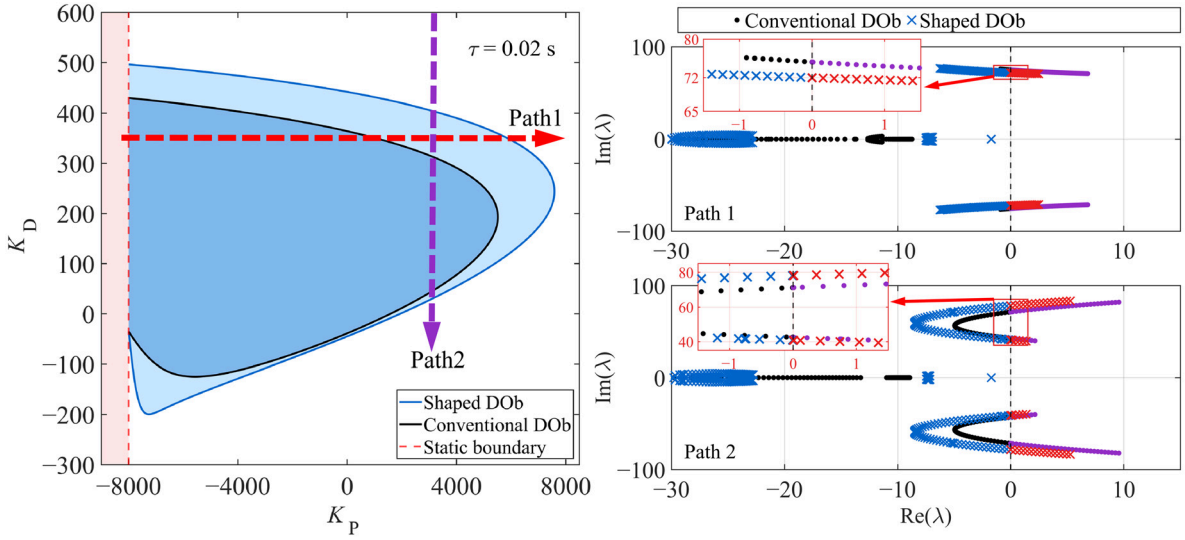


Figure 10. D-curves and characteristic-root trajectories along representative gain paths. **Left**: blue and black curves show the Shaped and Conventional DOb stability boundaries; darker shading indicates overlapping stable regions. The vertical red dashed line marks the static boundary. Red and purple arrows indicate Path 1 ($K_D = 350$, increasing K_P) and Path 2 ($K_P = 3000$, decreasing K_D), respectively. **Right**: black/purple dots denote stable/unstable Conventional DOb roots, while blue/red crosses denote stable/unstable Shaped DOb roots. Vertical dashed lines mark the imaginary axis; red boxes indicate regions enlarged in the insets.

Path 1 fixes $K_D = 350$ and increases K_P. The Shaped DOb roots cross into the right half-plane at a higher proportional gain, shifting the positive stability limit from $K_P = 1052.31$ to 5868.60, i.e., stability is maintained over a wider proportional gain range. Within the positive-gain domain, the admissible K_P interval expands from $(0, 1052.31)$ to $(0, 5868.60)$, a 457.7% increase. Path 2 fixes $K_P = 3000$ and decreases K_D. The critical roots move from the right half-plane to the left and then return, corresponding to instability, stability, and renewed instability. The Shaped DOb shifts the upper and lower boundaries from 315.94 and 41.71 to 406.12 and 27.24, respectively, increasing the stable K_D interval width from 274.23 to 378.88, a 38.2% increase.

By reshaping the compensation channel, the Shaped DOb delays critical root crossings and enlarges the stable controller range while maintaining disturbance estimation capability.

Figure 11 compares the steering responses to a 1 mrad initial angle perturbation at $K_D = 1.5$, $L = 50$, and a feedback delay of 40 ms. At the nominal simulation setting $K_P = 50$, the oscillations decay in both configurations. At $K_P = 1091$, they grow with the conventional DOb and decay with the Shaped DOb. At $K_P = 1342$, they grow in both configurations. These responses agree with the continuous-time and sampled-data stability classifications at the three plotted gains.

Table 5 compares observer order and compensation shaping using current torque inputs throughout. All four configurations use identical plant parameters, feedback delay, and the same sampled-feedback model. The continuous-time limits are evaluated from the corresponding current-input characteristic equations. At $T_s = 5$ ms, filtering increases the sampled-data critical K_P from 933.66 to 1048.58 for the conventional observer, while shaping increases it from 650.32 to 1261.66 for the higher-order observer. The Shaped DOb achieves the highest critical K_P among all four configurations, exceeding that of the Filtered DOb by 20.3% and providing the widest admissible positive proportional gain range at the specified

derivative gain. Its contribution lies in coordinating higher-order disturbance estimation with compensation shaping: the former provides a wider raw estimation bandwidth, while the latter provides the main stability benefit.

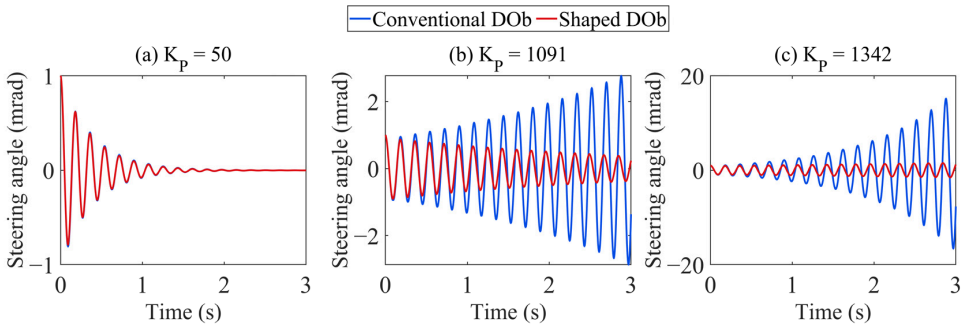


Figure 11. Steering-angle responses to an initial perturbation at three positive proportional gains with $K_D = 1.5$.

Table 5. Continuous-time and sampled-data critical proportional gains with current torque inputs at $K_D = 1.5$, $L = 50$, and a feedback delay of 40 ms.

Configuration	Continuous-Time Critical K_P	Sampled-Data Critical K_P
Conventional DOb	945.03	933.66
Filtered DOb	1080.89	1048.58
Unshaped DOb	648.20	650.32
Shaped DOb	1280.84	1261.66

Using identical current torque inputs and the same gain window, an independent sampled-feedback verification at $\tau = 0.04$ s and $L = 50$ gives a 57.6% larger stability region area for the Shaped DOb than for the Conventional DOb, supporting the qualitative trend in Figure 5.

The Shaped DOb could serve as a wheel-level steering controller within autonomous-vehicle motion-planning [36] and fault-tolerant motion control frameworks [37]. Its delay-dependent stability boundaries could guide steering-gain selection when executing vehicle-level commands. Such integration requires consideration of actuator limits and faults, followed by vehicle-level validation.

6. Conclusions

This study examines the coupling between disturbance compensation and vibration stability in DOb controlled distributed steer-by-wire corner modules with feedback delay. Although a DOb provides cost-effective wheel-end disturbance estimation and compensation, it also changes the compensation dynamics and characteristic root distribution. A Shaped DOb is proposed to improve time-varying disturbance tracking while enlarging the stability region. The main conclusions are:

1. The proposed Shaped DOb combines disturbance torque and disturbance rate estimation with a shaping filter, coordinating time-varying disturbance tracking with stability under feedback delay.
2. The D-curve and characteristic root analyses show that the Shaped DOb reduces the stability region contraction caused by feedback delay and increasing observer gain. The stability region area is increased by between 8.3% and 91.4%.
3. Under the common nominal pole setting, the Shaped DOb yielded smaller estimation phase lag than the conventional DOb at all four tested frequencies. Its RMSE was lower

at 0.5 and 1 Hz and higher at 2 and 5 Hz. The Shaped and Unshaped DObs yielded similar raw estimates.

The analytical results apply to a nominal linear steering model with fixed mechanical parameters, ideal torque actuation, and constant feedback delay. Parameter uncertainty, actuator dynamics, time-varying delays, backlash, saturation, and nonlinear or flexible effects require further validation. The present measurement noise analysis focuses on the nominal compensation channels.

Author Contributions: Conceptualization, C.S. and Z.L.; methodology, C.S., Z.L., and N.Z.; software, C.S. and H.S.; writing—original draft preparation, C.S., Z.L., and N.Z.; review and editing, N.Z. and H.S. All authors have read and agreed to the published version of the manuscript.

Funding: This work was supported by the National Natural Science Foundation of China under Grant Nos. 52572439 and 52394263 and the Yangzhou University Jiangdu High-end Equipment Engineering Technology Research Institute Innovation Capability Construction Project under Grant No. YDJD202504.

Institutional Review Board Statement: Not applicable.

Informed Consent Statement: Not applicable.

Data Availability Statement: The original contributions presented in this study are included in the article. Further inquiries can be directed to the corresponding author.

Conflicts of Interest: The authors declare no conflicts of interest.

Appendix A. Shaped DOb Error Convergence and Transfer Function Derivation

The aligned-input convergence analysis defines the nominal pole reference. With current torque input, $u(t) - u(t-\tau)$ additionally drives the estimation errors, and stability is assessed using the complete coupled closed-loop model.

Equation (9) gives the observer state dynamics. The Shaped DOb adds disturbance rate estimation to improve time-varying disturbance tracking:

$$T_{\mathrm{d}}(t+T_{\mathrm{s}}) = T_{\mathrm{d}}(t) + T_{\mathrm{s}}\dot{T}_{\mathrm{d}}(t) + O\left(T_{\mathrm{s}}^2\right), \tag{A1}$$

where T_{s} is the disturbance prediction interval and is set equal to the wheel-end controller sampling period. It must be much smaller than the dominant corner module and filter time constants to ensure a valid first-order Taylor approximation. Here, $T_{\mathrm{s}} = 0.005$ s.

The nominal continuous-time observer uses measurements and control input with the same delay τ. Define $d_\tau(t) = T_{\mathrm{d}}(t-\tau)$. Based on the nominal steering system model, the observer residual is defined as:

$$r_S(t) = \frac{\hat{T}_{\mathrm{d}}(t) + T_{\mathrm{SM}}(t-\tau) - C_{\mathrm{w}}\dot{\theta}_\tau(t) - K_{\mathrm{w}}\theta_\tau(t)}{J_{\mathrm{w}}}. \tag{A2}$$

To analyze the convergence of the observer, two estimation errors are defined:

$$\begin{aligned} e_1(t) &= d_\tau(t) - \hat{T}_d(t) \\ e_2(t) &= \dot{d}_\tau(t) - \dot{\hat{T}}_d(t). \end{aligned} \tag{A3}$$

The corresponding error dynamics are expressed as:

$$\begin{bmatrix} \dot{e}_1 \\ \dot{e}_2 \end{bmatrix} = \begin{bmatrix} -\frac{L_1}{J_w} & 1 \\ -\frac{L_2}{J_w} & 0 \end{bmatrix} \begin{bmatrix} e_1 \\ e_2 \end{bmatrix} + \begin{bmatrix} 0 \\ \ddot{d}_\tau \end{bmatrix}. \tag{A4}$$

where for $L_1 > 0$ and $L_2 > 0$, the error system matrix is Hurwitz. Consequently, the homogeneous estimation errors decay asymptotically, while the second derivative of the delayed disturbance acts as an external input to the error dynamics.

To define a common nominal error-pole location for observer tuning, the pole of the conventional DOb is written as follows:

$$s_D = -\frac{L}{J_w}. \tag{A5}$$

Placing the two observation error poles of the Shaped DOb at sD gives the desired characteristic polynomial:

$$\left(s + \frac{L}{J_w}\right)^2 = s^2 + \frac{2L}{J_w}s + \frac{L^2}{J_w^2}. \tag{A6}$$

Using the reference pole in Equation (A5), matching the characteristic polynomial of the error system in Equation (A4) to the desired polynomial in Equation (A6) gives $L_1 = 2L$ and $L_2 = L^2/J_{\mathrm{w}}$. For smooth disturbances, assume that the first and second derivatives of T_{d} are bounded by M_1 and M_2. Under the matched-pole configuration with $\omega_{\mathrm{o}} = L/J_{\mathrm{w}}$, the nominal error dynamics satisfy:

$$\ddot{e}_1 + 2\omega_o\dot{e}_1 + \omega_o^2 e_1 = \ddot{d}_\tau. \tag{A7}$$

The impulse response t $\exp(-\omega_{\mathrm{o}}\, t)$ has integral $1/{\omega_{\mathrm{o}}}^2$. Including the current-to-delayed disturbance mismatch gives:

$$\limsup_{t\to\infty}\left|T_d(t) - \hat{T}_d(t)\right| \le \tau M_1 + \frac{M_2}{\omega_o^2}. \tag{A8}$$

For a sinusoidal disturbance of amplitude A and angular frequency Ω, $M_2 = \mathrm{A}\Omega^2$. Higher frequencies therefore increase the curvature forcing and error bound. Ideal step inputs are analyzed piecewise.

For the augmented model, the shaping filter states $q_1(t)$ and $q_2(t)$ are introduced as:

$$\begin{cases} \dot{q}_1(t) = q_2(t) \\ \dot{q}_2(t) = \frac{\hat{T}_{\mathrm{d}}(t) - q_1(t) - \left(T_{\mathrm{p1}} + T_{\mathrm{p2}}\right)q_2(t)}{T_{\mathrm{p1}}T_{\mathrm{p2}}}. \end{cases} \tag{A9}$$

Appendix B. Derivation of the Closed-Loop Time Delay Model with the Conventional DOb

Expanding and rearranging Equation (20) gives the scalar characteristic equation of the closed-loop system with the conventional DOb:

$$\Delta_{\mathrm{D}}(\lambda) = \left(\lambda + \frac{L}{J_{\mathrm{w}}}e^{-\lambda\tau}\right)\left(\lambda^2 + \frac{C_{\mathrm{w}}}{J_{\mathrm{w}}}\lambda + \frac{K_{\mathrm{w}}}{J_{\mathrm{w}}}\right) + \frac{e^{-\lambda\tau}}{J_{\mathrm{w}}}\left(\lambda + \frac{L}{J_{\mathrm{w}}}\right)(K_{\mathrm{P}} + K_{\mathrm{D}}\lambda) = 0, \tag{A10}$$

where the term independent of the controller gains is:

$$d_{0,\mathrm{D}} = [Lc_1 + \mathrm{i}(\omega - Ls_1)][a(\omega) + \mathrm{i}b(\omega)]. \tag{A11}$$

Therefore, define:

$$\begin{cases} r_{0,\mathrm{D}} = Lc_1 a - (\omega - Ls_1)b \\ s_{0,\mathrm{D}} = Lc_1 b + (\omega - Ls_1)a. \end{cases} \tag{A12}$$

The coefficient of the proportional gain is:

$$d_{\mathrm{P,D}} = \frac{e^{-\mathrm{i}\omega\tau}}{J_{\mathrm{w}}}(\mathrm{i}\omega + L), \tag{A13}$$

where the real and imaginary parts are expressed as:

$$\begin{cases} r_{\mathrm{P,D}} = \frac{Lc_1+\omega s_1}{J_{\mathrm{w}}} \\ s_{\mathrm{P,D}} = \frac{\omega c_1 - Ls_1}{J_{\mathrm{w}}}. \end{cases} \tag{A14}$$

The coefficient of the derivative gain is:

$$d_{\mathrm{D,D}} = \mathrm{i}\omega d_{\mathrm{P,D}}. \tag{A15}$$

Therefore, define:

$$\begin{cases} r_{\mathrm{D,D}} = -\omega s_{\mathrm{P,D}} \\ s_{\mathrm{D,D}} = \omega r_{\mathrm{P,D}}. \end{cases} \tag{A16}$$

Appendix C. Derivation of the Closed-Loop Time Delay Model with the Shaped DOb

Substituting the shaped compensation torque in Equation (14) into the steering dynamics and combining the Shaped DOb error and filter state equations gives the closed-loop estimation error subsystem. For homogeneous stability analysis, $T_{\dot{\mathrm{d}}0} = 0$ and $T_{\ddot{\mathrm{d}}0} = 0$:

$$\begin{cases} \dot{e}_1(t) = e_2(t) - \frac{L_1}{J_{\mathrm{w}}}\left[e_1(t) + \bar{q}_1(t) + T_z\bar{q}_2(t)\right] - \frac{L_1}{J_{\mathrm{w}}}\left[K_{\mathrm{D}}\dot{\theta}(t-\tau) + K_{\mathrm{P}}\theta(t-\tau)\right] \\ \quad + \frac{L_1}{J_{\mathrm{w}}}\left[\bar{q}_1(t-\tau) + T_z\bar{q}_2(t-\tau)\right] + \frac{L_1}{J_{\mathrm{w}}}\left[K_{\mathrm{D}}\dot{\theta}(t-2\tau) + K_{\mathrm{P}}\theta(t-2\tau)\right] \\ \dot{e}_2(t) = -\frac{L_2}{J_{\mathrm{w}}}\left[e_1(t) + \bar{q}_1(t) + T_z\bar{q}_2(t)\right] - \frac{L_2}{J_{\mathrm{w}}}\left[K_{\mathrm{D}}\dot{\theta}(t-\tau) + K_{\mathrm{P}}\theta(t-\tau)\right] \\ \quad + \frac{L_2}{J_{\mathrm{w}}}\left[\bar{q}_1(t-\tau) + T_z\bar{q}_2(t-\tau)\right] + \frac{L_2}{J_{\mathrm{w}}}\left[K_{\mathrm{D}}\dot{\theta}(t-2\tau) + K_{\mathrm{P}}\theta(t-2\tau)\right]. \end{cases} \tag{A17}$$

Using an affine numerical formulation, the characteristic determinant can be expressed as:

$$\Delta_{\mathrm{SH}}(\mathrm{i}\omega) = d_{0,\mathrm{SH}} + d_{\mathrm{P,SH}}K_{\mathrm{P}} + d_{\mathrm{D,SH}}K_{\mathrm{D}}, \tag{A18}$$

where

$$\begin{aligned} d_{0,\mathrm{SH}} &= \Delta_{\mathrm{SH}}(\mathrm{i}\omega, 0, 0) \\ d_{\mathrm{P,SH}} &= \Delta_{\mathrm{SH}}(\mathrm{i}\omega, 1, 0) - d_{0,\mathrm{SH}} \\ d_{\mathrm{D,SH}} &= \Delta_{\mathrm{SH}}(\mathrm{i}\omega, 0, 1) - d_{0,\mathrm{SH}}. \end{aligned} \tag{A19}$$

Based on its affine dependence on K_{P} and K_{D}, the characteristic determinant is rearranged as:

$$\begin{aligned} d_{0,\mathrm{SH}} &= r_{0,\mathrm{SH}} + \mathrm{i}s_{0,\mathrm{SH}} \\ d_{\mathrm{P,SH}} &= r_{\mathrm{P,SH}} + \mathrm{i}s_{\mathrm{P,SH}} \\ d_{\mathrm{D,SH}} &= r_{\mathrm{D,SH}} + \mathrm{i}s_{\mathrm{D,SH}}. \end{aligned} \tag{A20}$$

References

1. Schmitz, T. Chassis concept of the individually steerable five-link suspension: A novel approach to maximize the road wheel angle to improve vehicle agility. *Automot. Engine Technol.* **2024**, *9*, 5. [CrossRef]
2. Qiao, Y.; Chen, X.; Yin, D. Coordinated control for the trajectory tracking of four-wheel independent drive–four-wheel independent steering electric vehicles based on the extension dynamic stability domain. *Actuators* **2024**, *13*, 77. [CrossRef]
3. Lu, Y.; Zhong, J.; Khoshnevisan, L.; Sun, C.; Khajepour, A. A review on vehicle steer-by-wire control systems. *Veh. Syst. Dyn.* **2025**. *Online first*. [CrossRef]
4. Wang, H.; Wang, Y.; Pi, D.; Yan, Y.; Li, X.; Fan, D.; Zhang, C.; Zhang, P. Research on steering-by-wire mode switching and control method of corner module vehicle. *Proc. Inst. Mech. Eng. Part D J. Automob. Eng.* **2026**. *Online first*. [CrossRef]
5. Sung, Y.M.; Lee, J.P.; Cho, J.M. Model-based yaw-rate tracking control with online adaptation of steering and tire parameters for an e-corner-based four-wheel independent steering vehicle. *J. Auto. -Veh. Saf. Assoc.* **2026**, *18*, 110–126. [CrossRef]
6. Geng, G.; Sun, D.; Ma, J.; Li, H. Adaptive sliding mode control based on a peak-suppression extended state observer for angle tracking in steer-by-wire systems. *Actuators* **2026**, *15*, 128. [CrossRef]
7. Lv, S.; Leng, H.; Zhang, F. Adaptive sliding mode trajectory tracking control for four-wheel independent steering vehicles based on instantaneous center of rotation constraints. *World Electr. Veh. J.* **2026**, *17*, 330. [CrossRef]

8. Zhou, G.; Fang, Z.; Li, D.; Jin, Y.; Wang, Y. Synchronization and tracking control strategy of four-wheel independent steering system based on improved model predictive control method. *ISA Trans.* **2025**, *166*, 89–102. [CrossRef] [PubMed]
9. Hu, Y.; Song, J.; Dong, H.; Miura, Y.; Ji, X. A DOB–MPC steering angle tracking control strategy with explicit compensation of steering load and internal friction. *Adv. Eng. Inform.* **2026**, *76*, 105087. [CrossRef]
10. Khazal, H.; Alanazi, A.O.; Khdir, Y.K.; Firouzi, N.; Podulka, P. Optimal disturbance-observer-based fuzzy PID back-stepping control of a self-driving car with a steer-by-wire system. *Vehicles* **2026**, *8*, 124. [CrossRef]
11. Gao, Y.; Wang, W.; Yang, C.; Zhang, Y.; Qie, T.; Ma, T. A new reaching law for anti-disturbance sliding mode control of steer-by-wire system. *IEEE Trans. Veh. Technol.* **2025**, *74*, 4064–4075. [CrossRef]
12. Gao, Y.; Yang, C.; Zhang, Y.; Wang, W.; Yan, Q. Neural network-based adaptive inverse fuzzy control for steer-by-wire system considering steering hysteresis. *Control Eng. Pract.* **2026**, *175*, 107121. [CrossRef]
13. Liu, H.; Li, J.; Ji, X.; Liu, Y. Design of a robust angle tracking controller for steering-by-wire systems with angular velocity observer and friction compensation. *Control Eng. Pract.* **2025**, *163*, 106402. [CrossRef]
14. SariyiLiz, E. A high performance disturbance observer. In *2025 IEEE International Conference on Mechatronics*; IEEE: New York, NY, USA, 2025; pp. 1–6. [CrossRef]
15. SariyiLiz, E.; Ohnishi, K. Stability and robustness of disturbance-observer-based motion control systems. *IEEE Trans. Ind. Electron.* **2015**, *62*, 414–422. [CrossRef]
16. Sariyildiz, E.; Hangai, S.; Uzunovic, T.; Nozaki, T.; Ohnishi, K. Stability and robustness of the disturbance observer-based motion control systems in discrete-time domain. *IEEE/ASME Trans. Mechatron.* **2021**, *26*, 2139–2150. [CrossRef]
17. Li, Z.; Zhang, N.; Lu, H.; Ye, F.; Wang, C. Impacts of the observation of the steering torque disturbance on the stability of a time-delayed control system for a corner module with steering. *Actuators* **2025**, *14*, 518. [CrossRef]
18. Xu, Z.; Shi, Q.; Wei, Y.; Zheng, X.; Huang, C.; He, L. Angle demand control of steer-by-wire system by disturbance estimation-based generalized predictive control approach. *Proc. Inst. Mech. Eng. Part I J. Syst. Control Eng.* **2024**, *238*, 608–620. [CrossRef]
19. Zhao, X.; Zhao, L. Steering angle tracking control of steer-by-wire system with prescribed performance under primary sensor failure. *Control Eng. Pract.* **2025**, *161*, 106354. [CrossRef]
20. Ayati, M.; Sajjadi, M.B.; Esmaeilzadeh, M.; Abrinia, K.; Keshavarz-Mohammadian, A. Fast disturbance observer-based adaptive integral terminal sliding mode control for a vehicle steer-by-wire system. *Asian J. Control* **2026**, 1–13. [CrossRef]
21. Castillo-Frasquet, A.; García, P.J. Predicting the future state of disturbed LTI systems: A solution based on high-order observers. *Automatica* **2021**, *124*, 109365. [CrossRef]
22. Joo, Y. Performance recovery and stability analysis of disturbance observer under unmodeled dynamics. *Sensors* **2024**, *24*, 7850. [CrossRef] [PubMed]
23. Herbst, G.; Hempel, A.J. Half-gain observer tuning for noise reduction in discrete-time ADRC. *Control Eng. Pract.* **2025**, *164*, 106501. [CrossRef]
24. Jeong, H.; Suk, J.; Kim, S. Control of quadrotor UAV using variable disturbance observer-based strategy. *Control Eng. Pract.* **2024**, *150*, 105990. [CrossRef]
25. Chang, H.; Song, D.; Lee, C.; Shim, H. Robust stability condition and simplified design of filter-embedded disturbance observer. *Int. J. Control Autom. Syst.* **2024**, *22*, 3584–3594. [CrossRef]
26. Rim, S.Y.; Yun, J.N.; Hwang, C.J.; Kim, J.R. A determination method of LPFs for robust stability of DOB/CDOB-based control system. *Int. J. Dyn. Control* **2025**, *13*, 193. [CrossRef]
27. Jin, Q.; Cai, W.; Du, X. Improved disturbance observer-based control for multivariable processes with time delays based on modified inverse model. *Trans. Inst. Meas. Control* **2020**, *42*, 339–350. [CrossRef]
28. Tena, D.; Peñarrocha-Alós, I.; Sanchis, R. Performance, robustness and noise amplification trade-offs in disturbance observer control design. *Eur. J. Control* **2022**, *65*, 100630. [CrossRef]
29. Zhang, N.; Li, Z.; Wang, C.; Wang, J.; Zhuang, W.; Wei, W.; Yin, G. A state-of-the-art review on the revolution of structure and control of vehicle chassis system: From tradition to distributed chassis system. *Chin. J. Mech. Eng.* **2025**, *38*, 128. [CrossRef]
30. Lee, Y.C.; Huang, C.C.; Malepati, U.; Zhou, X.; Wang, J. Practical method for high-speed path-tracking control of vehicles with time-delayed steering system dynamics. *IEEJ J. Ind. Appl.* **2026**, *15*, 42–53. [CrossRef]
31. Su, J.; Chen, W.H.; Li, B. High order disturbance observer design for linear and nonlinear systems. In *2015 IEEE International Conference on Information and Automation*; IEEE: New York, NY, USA, 2015; pp. 1893–1898. [CrossRef]
32. Yang, J.; Hu, C.; Zhu, Y.; Wang, Z.; Zhang, M. Experimental investigation of shaping disturbance observer design for motion control of precision mechatronic stages with resonances. *Mech. Syst. Signal Process.* **2017**, *92*, 334–348. [CrossRef]
33. Moosapour, S.H.; Ataei, M.; Ekramian, M. Prediction-based sliding mode control of non-linear systems with input delay using disturbance observer. *IET Control Theory Appl.* **2019**, *13*, 2047–2055. [CrossRef]
34. Chen, W.H. Disturbance observer based control for nonlinear systems. *IEEE/ASME Trans. Mechatron.* **2004**, *9*, 706–710. [CrossRef]
35. Chen, X.P.; Dai, H. Stability analysis of time-delay systems using a contour integral method. *Appl. Math. Comput.* **2016**, *273*, 390–397. [CrossRef]

36. Huang, T.; Pan, H.; Sun, W.; Gao, H. Sine resistance network-based motion planning approach for autonomous electric vehicles in dynamic environments. *IEEE Trans. Transp. Electrif.* **2022**, *8*, 2862–2873. [CrossRef]
37. Huang, T.; Wang, J.; Pan, H.; Sun, W. Finite-time fault-tolerant integrated motion control for autonomous vehicles with prescribed performance. *IEEE Trans. Transp. Electrif.* **2022**, *9*, 4255–4265. [CrossRef]

Disclaimer/Publisher's Note: The statements, opinions and data contained in all publications are solely those of the individual author(s) and contributor(s) and not of MDPI and/or the editor(s). MDPI and/or the editor(s) disclaim responsibility for any injury to people or property resulting from any ideas, methods, instructions or products referred to in the content.